Proceedings: Computational Modeling of Materials, Minerals and Metals Processing, Cross, Bailey, Evans, eds.,
(Conference in Seattle, WA, Feb. 18-20,2002), The Mater., Minerals, & Metals Soc., Warrendale, PA, 2001, pp. 491-500.

SIMULATION OF TURBULENT FLOW AND PARTICLE TRANSPORT IN THE CONTINUOUS CASTING OF STEEL

Q. Yuan, T. Shi, S. P. Vanka, and B.G. Thomas

Department of Mechanical and Industrial Engineering
University of Illinois at Urbana-Champaign
1206 W Green Street, Urbana, IL. 61801 USA
bgthomas@uiuc.edu

Abstract

The quality of continuous cast steel is greatly affected by fluid flow in the mold region, especially involving transient phenomena. Mathematical models are being applied to investigate many different aspects of these phenomena, but their accuracy must be validated before they can be applied with confidence. As part of a long-term effort to develop and apply comprehensive models of the continuous casting process, this work evaluates the relative accuracy of models of three different fluid flow phenomena in continuous casting through comparison with measurements.

Firstly, transient flow simulations of velocities in the mold region are compared with digital particle image velocimetry (PIV) measurements in a single phase water model. Large-eddy simulations (LES) are found to reasonably match the flow measurements, including transient flow variations, except at long time scales, which could not be modeled owing to the excessive computation costs. The standard K-ε model produced very good agreement with time-averaged velocities for relatively little computation time, although it is inaccurate at predicting the transient variations. Secondly, particle trajectory calculations are compared with water model measurements to study the distribution and flotation removal of inclusion particles. The LES model was able to match the measurements both qualitatively and quantitatively. Thirdly, steady, multiphase flow computations are compared with flow patterns observed in both a water model and an operating steel caster with argon gas injection. For the same conditions, the water model and steel caster produced very different flow behavior. The computational model was able to match the measured flow patterns in both cases.

This work suggests that computational flow modeling has the potential to match real processes as well or better than water models, especially when complex related phenomena such as particle motion and multiphase flow are involved. Much work is still needed to further improve the models and to apply them in parametric studies.

Single-Phase Fluid Flow Study

Flow visualization and velocity measurements were made using 0.4-scale Plexiglas water models of the tundish, nozzle and mold region of the caster at LTV Steel Technology Center for the conditions given in Table 1 and illustrated in Figure 1. Sequences of instantaneous velocity vector distributions were measured using a PIV system.[1, 2] Velocities in the strand water model were then computed with two Large Eddy Simulations (LES) [2, 3] and a standard K-ε model, based on CFX 4.2 [4], for conditions given in Table I. Only half of the mold was computed with the three-dimensional models, assuming symmetry about the central vertical plane.

The first LES computation employed the Smagorinsky subgrid model for the turbulent viscosity and adopted inlet velocities into the mold from a prior LES simulation of an approximate nozzle, consisting of a turbulent pipe flow calculation with a partially blocked inlet, fed into a rectangular duct section. The second LES simulation employed no subgrid model (so is a coarse-grid DNS simulation). It simply adopted inlet velocities at the nozzle port from an LES computation of fully-developed, nonswirling, turbulent flow in a square duct [2, 5]. In both cases, the unsteady inlet velocity profiles were rotated 30° downward to match the jet angle observed exiting the actual nozzle. The K-ε simulation employed steady inlet conditions from a separate model of the nozzle.[6] The K-ε model has a great computational savings over the fine-mesh LES model, which requires several weeks of CPU time for a single computation. Further details on the computational methods are provided elsewhere.[3, 5]

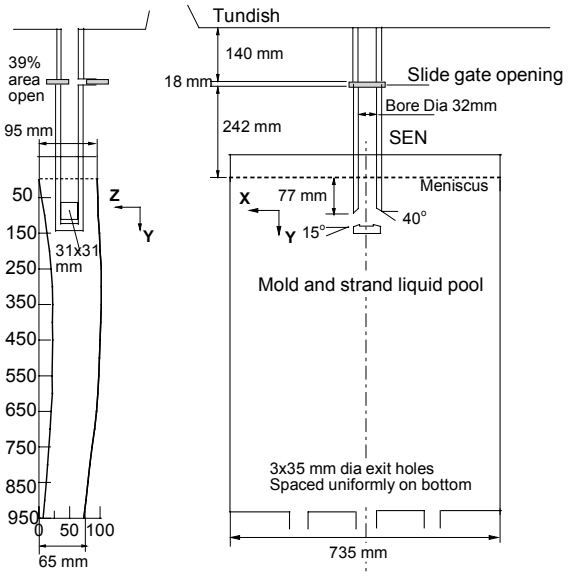

Figure 1: Schematic of the 0.4-scale water model.

Table I 0.4-scale water model conditions and dimensions.

Dimensions/Condition	Value
Slide-gate orientation	90°
Slide-gate opening, linear fraction	52%
SEN bore diameter	32mm
SEN submergence depth	77 ± 3mm
Port Height × Width	32mm × 31mm
Port thickness	11mm
Port angle, lower edge	15° down
Port angle, upper edge	40° down
Bottom well recess depth	4.8mm
Water model height	950mm
Water model width	735mm
Water model thickness	80 mm ± 15 mm
Inlet volumetric flow rate through each port	3.53×10^{-4} m^3/s
Averaged inlet jet angle at port	30°
Liquid density	1000 kg/m^3
Liquid material viscosity	0.001 Pa-s
Gas injection	0%

The time-averaged velocity fields at the center plane between the wide faces obtained from the LES1, LES2, and K-ε models and the PIV measurements are all shown in Figure 2 to have a classic pair of simple recirculation zones in each half of the caster mold. Only some of the velocity vectors for the two LES computations are plotted to make the plot resolutions comparable to the PIV measurement. The jet from the nozzle plane impinges against the narrow face and splits. The upward flow along the narrow face moves back across the top surface towards the inlet, forming a recirculation region called the upper roll. The downward flow is deflected by the bottom of the water model around and up the center symmetry plane, to form a relatively stable recirculation region below the jet, called the lower roll. Both the LES velocity fields were time averaged over 45s. The LES1, PIV and K-ε jets all bend slightly upward as they traverse across the mold, producing similar flow patterns. LES2 has a straighter jet, likely due to neglecting the swirl in the inlet flow.

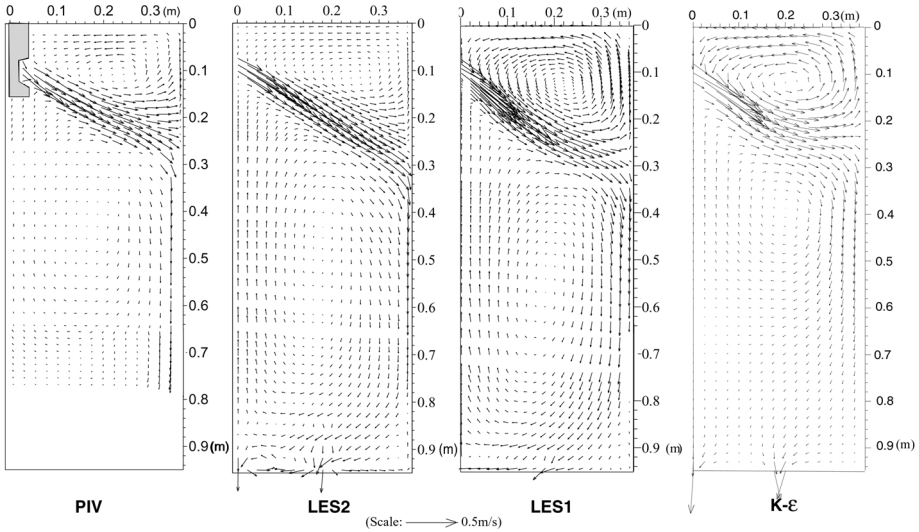

Figure 2: Time-averaged velocity fields at the center plane.

The time-averaged fluid speeds $\left(\bar{v}_x + \bar{v}_y\right)^{1/2}$ from all four methods, LES1, LES2, PIV and K-ε are compared quantitatively in Figures 3 and 4. Speed profiles along the jet centerline, defined by the location of maximum speed $\left(\bar{v}_x + \bar{v}_y\right)^{1/2}$ are compared in Figure 3. The jet speed consistently decreases as it approaches the narrow face, as the jet entrains fluid and diffuses its momentum away from the centerline. All of the computed slopes agree with the three consistent sets of PIV measurements. The LES1 results have the best quantitative agreement with the PIV measurements. The speeds from LES2 are consistently higher than the measurements by 0.05m/s to 0.1m/s, likely due to its lack of the observed swirling flow causing less entrainment. The K-ε jet velocities are consistently a little low, due to overprediction of the turbulence and its accompanying momentum dissipation.

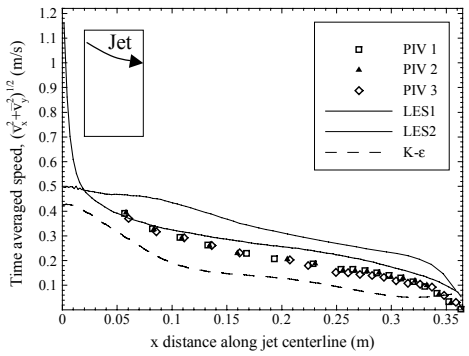

Figure 3: Time-averaged velocity along jet centerline.

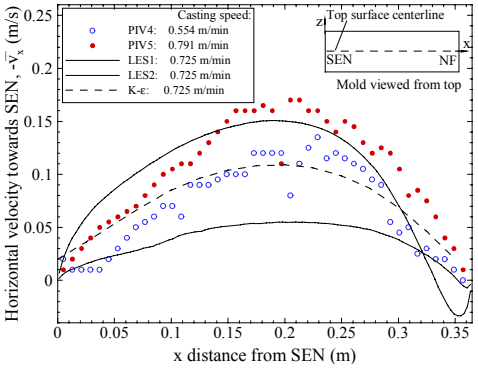

Figure 4: Time averaged velocity along top surface centerline.

Figure 4 compares the time-averaged horizontal speeds along the top surface centerline, (taken about 1.5mm below the top surface). In all cases, fluid flows from the narrow face towards the SEN, with the maximum velocity occurring at approximately half way between. Quantitatively, the LES1and K-ε velocities are seen to reasonably match the two sets of PIV measurements. The velocities obtained from LES2 are consistently smaller. This is believed to be caused by the straighter jet of this simulation, which impinges at a steeper angle against the narrow face, and thus deflects less flow upwards.

The transient nature of the flow is illustrated by the sample time histories in Figure 5, which compares the LES1, LES2, and PIV horizontal velocity histories found at a point located 1.5 mm below the top surface, midway between the narrow face and SEN. Transient behavior is very important to quality in continuous casting. This particular point is of special interest because an

excessive value of this maximum surface velocity could cause entrainment of the top surface liquid slag. The PIV data points are 0.2s apart, while the LES computations have 0.001s - 0.0005s increments, so appear continuous. At least two time scales are seen in both the computations and measurements. The short time scale fluctuations obtained from the computations are around 0.7s, which agrees well with the PIV measurements. The longer time scale obtained from the PIV measurement is at least 45s, with the horizontal velocity increasing to almost twice its mean value for time intervals of over 5 s. This long time scale fluctuation is not very clear in the computations, although a slight variation can be seen with a 25s – 45s period. A longer time sampling might be required to fully capture the longer time scale. In addition, a full-width computation might be required to capture the larger magnitude of the real long-time scale fluctuations at this important location.

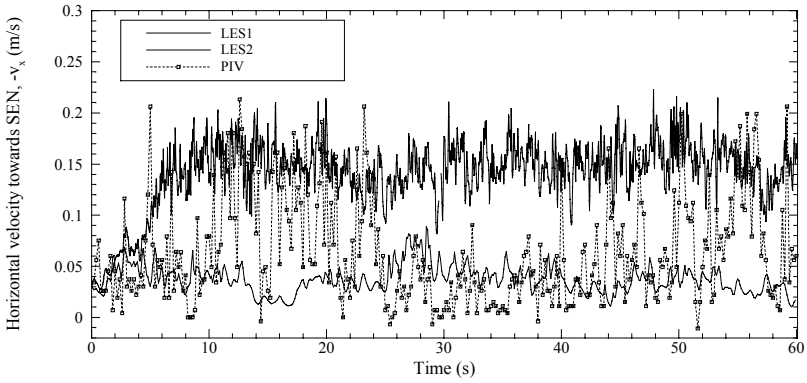

Figure 5: Horizontal velocity variations at a sample point located near the top surface, half way between SEN and narrow face.

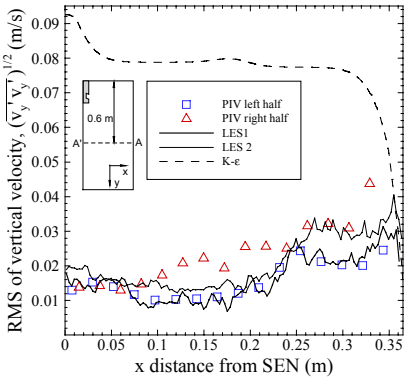

Figure 6: RMS of upward velocity along a line in lower roll region.

Velocity variations can be characterized by their root mean square values (RMS), which is defined by $\left(\frac{1}{\Delta t}\int_{t_1}^{t_2} v_y'^{\,2}\,dt\right)^{1/2}$, where Δt is the interval for the time averaging ($\Delta t = t_2 - t_1$). The RMS of the downward velocity is shown in Figure 6 along the line 0.6m below the top surface at the center plane. Both the LES results match remarkably well with the measurements, indicating that LES models are capable of accurately predicting this measure of transient variations due to turbulence. The K-ε prediction of this RMS distribution is seen to disagree both qualitatively and quantitatively. This result cautions that the crude isotropic, steady measure of turbulence of the K-ε model needs further calibration or adjustment before it can be reliably interpreted for turbulence predictions, such as level fluctuations or particle collision rates.

Particle Transport Study

Particles such as alumina inclusions, which are carried in with the jet entering the mold, may cause serious defects in the final steel product if they are not able to float harmlessly into the top-surface slag layer. The LES computations were extended to study both fluid flow and particle transport in the mold region of a full-scale water model[7] for conditions given in Table II. Particle transport experiments[7] were performed in the water model by injecting 8000-30000 elliptical disk-shaped plastic beads with the water through the nozzle into the mold in each of at least five experiments. The density and size of the beads were chosen to match the vertical terminal velocity of 300μm alumina inclusions in molten steel. A screen was positioned near the top surface to trap the plastic beads and thereby simulate the removal of inclusion particles to the top surface. The average removal fraction was reported at different time intervals[7]. A hot-wire anemometer was used to measure the fluid velocity field.[8]

Table II. Parameters for full-scale water model particle experiment.

Dimensions/conditions	Value
Port height × width	0.051m × 0.056 m
Submergence depth	0.150m
Nozzle angle	25° down
Inlet jet angle	25° down
Water model height	2.152m
Water model width	1.83m
Water model thickness	0.238m
Average inlet flow rate	0.00344 m^3/s
Average inlet speed (m/s)	1.69
Casting speed	0.0152 m/s
Fluid density	1000 kg/m^3
Fluid kinematic viscosity	1.0×10^{-6} m^2/s
Particle inclusion size	2 – 3 mm
Particle inclusion density	988kg/m^3

For inlet conditions, the LES flow model adopted velocity profiles from a prior simulation of fully-developed turbulent-flow in a pipe, rotated to the 25˚ downward inlet angle observed in the water model. After quasi-steady flow conditions were achieved in the strand water model, a large group of 15,000 particles was introduced at random locations on the inlet plane over a 1.6 s time interval. Six further groups of 500 particles each were then introduced every 2 seconds over 0.4s intervals. The particles were assumed to be spherical and were given initial velocities equal to the local instantaneous fluid velocity. Each particle trajectory was tracked during the transient flow simulation using a Lagrangian approach, by integrating the particle transport equation with a fourth-order Runge-Kutta method at each time step, assuming a the density difference and a drag force for particle vertical buoyancy force according to Reynolds numbers up to 800.[9]

The computed fluid velocity field is very similar to the 0.4-scale water model results and agrees with flow observations of the full-scale water model.[8, 10] Figure 7 presents snapshots of the instantaneous distribution computed for the 15000 particles (group 0) at four different times after they were injected. The short line near the top surface represents the position of the screen. Neither the fluid flow nor the particle trajectory calculations are affected by the computational screen.

Figure 7 shows that the particles move with the jet after injection and start to impact the narrow face at about 1.6s. Next, they split into two groups and enter either the upper or lower recirculation rolls (Figure 7, 10s). Due in part to their buoyancy, many of the particles in the upper roll move to the top surface and are quickly and safely removed. Other particles circulate for a significant time (100s or more) before reaching the top surface to be removed. Finally, a few particles flow out of the mold bottom with the outflow and would be trapped at a deeper position, leading to defects in the real steel strand. Moreover, in a real steel caster, inclusion particles can also be entrapped by the solidifying shell (corresponding to the sidewalls of the water model). This was not modeled in either the water model or the computation.

Figure 8 shows the computed trajectories of four typical particles for 100 seconds, or until they contact the top surface (top left) or exit the domain (top right). The other two particles (lower frames) are still moving. These irregular trajectories show evidence of chaotic motion and illustrate the significant effect of the turbulent flow structures on particle transport, looking in both the wideface and narrow face directions.

The trajectory computations for the 15000-particles (group 0) were processed to compute the particle removal rate and removal fraction to the top surface (lines) in Figure 9 and to compare the computed and measured removal fractions by the screen (symbols). Removal is calculated by summing at each time step, the particles that touch either the top surface or the screen (from above). Considering the approximate nature of the experiments, and the uncertainties in the computations, the agreement between the computation and measurements appears to be quite good. Furthermore, the screen appears to simulate surface removal well at early times, but under-predicts it at later times (100s). The computation shows that the total removal rate appears to be very large (nearly 80%) when the walls do not trap particles. The initial positions of the particles in the nozzle port plane are found to be unrelated with their chance of removal to the top surface.

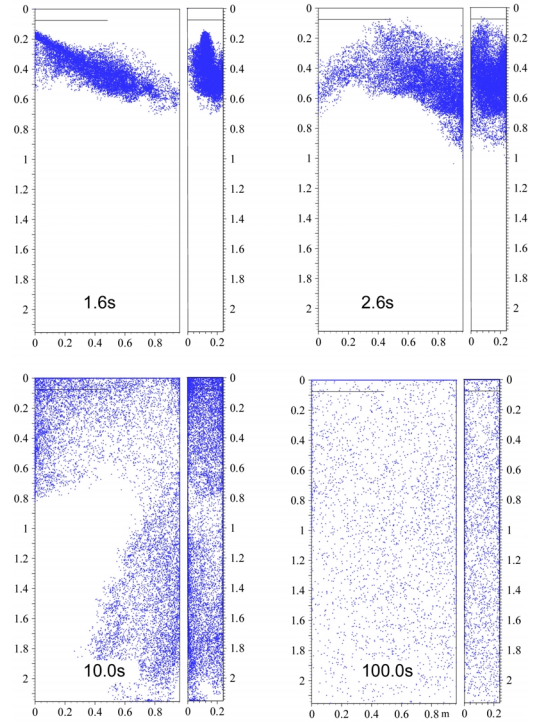

Figure 7: Distribution of the 15000 particles at four instants after their injection.

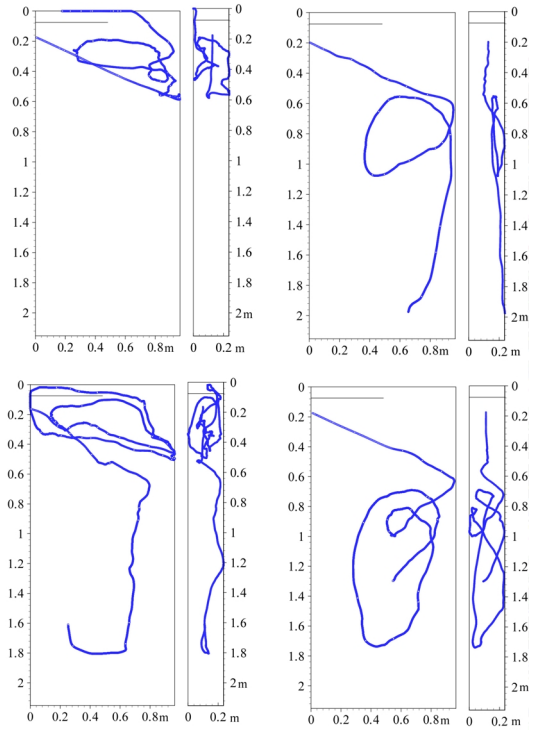

Figure 8: Four typical particle trajectories found in the computation.

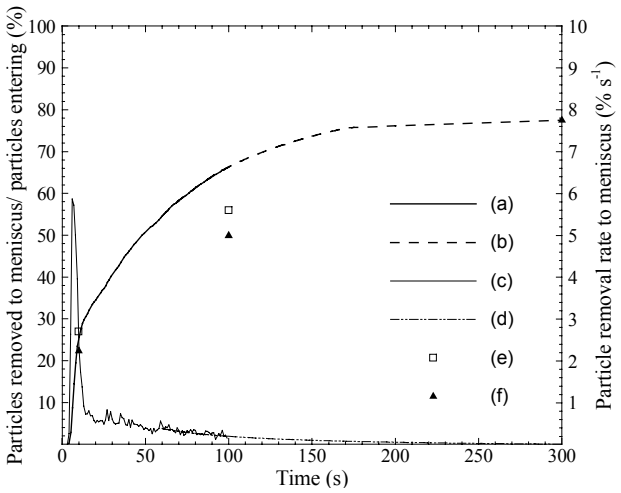

Figure 9: Particle removal to the top surface in full-scale water model: (a) particles removed to top surface (simulated); (b) particles removed to top surface; (c) particle removal rate to top surface; (d) particle removal rate to top surface; (e) particles removed by screen (LES); (f) particles removed by screen (experiment).

Table III: Comparison of particle removal by screen.

		0-10 seconds	10-100 seconds
LES	500 particle groups		
	1	27.2%	23.4%
	2	17.8%	27.2%
	3	26.2%	23.0%
	4	23.8%	23.2%
	5	33.0%	18.2%
	Average	25.56%	23.0%
	15000 particles (group 0)	26.96%	26.03%
Experiment		22.3%	27.6%

Finally, the computed particle removal fractions by the screen are compared in Table III with measurements. The removal rate of an individual group of 500 particles can be very different by a factor of over 1.5. This appears to be due to the sensitivity of the particle trajectories to transient variations in the flow field which persist over several seconds. However the average of 5 groups agrees with both the experiment and the 15000-particle group result. These results indicate that a large number of particles are required to study their transport (at least 2500 in this case), and that LES has the potential to accurately predict particle trajectories and removal. Its main drawback is slow computational speed, as this single simulation of 140s required 39 days

on a Pentium III 750 MHz PC for 175,000 time steps. Future work will investigate faster computational methods for parametric studies.

Multiphase Flow Study

Argon gas is often injected into the nozzle in order to prevent its clogging. This gas also has a great influence on flow in the strand. Increasing the amount of gas injection increases the buoyancy of the liquid jet, causing it to lift upward. Without gas, the classic "double roll" flow pattern is often produced, as studied in the previous section. Increasing the gas percentage above a critical level causes the flow pattern to change directions, forming a "single-roll" flow pattern, where the flow across the top surface is directed away from the SEN. This transition in flow patterns was studied using both water models and steady K-ε computations. In this work, a single set of conditions was studied, given in Table IV. This case was chosen because previous work had discovered discrepancies for these particular conditions between the flow patterns found in a 0.4-scale water model and in the actual caster, as measured both by electromagnetic sensors in the mold wall and as inferred by the shape of the slag layer.[1]

Table IV Multiphase Flow Model Conditions

	0.4-scale Water Model	Steel Caster
Mold Width x Thickness	730 x 80 mm	1854 x 228 mm
Mold / Strand Height	950 mm	open bottom
Nozzle Submergence Depth (top surface to top of port)	80 mm	165 mm (6.5 inch)
Nozzle Bore Inner Diameter	31 mm	80 mm
Port Wall Thickness	11mm	27.5 mm
Nozzle Port Height x Width	31 x 31 mm	78 x 78 mm
Nominal Vertical Angle of Port Edges	15° down	15° down
Jet Angle: vertical, horizontal	30˚ down 0˚	10.1˚ down 12.1˚
Average Inlet Velocities, V_x, V_z	0.358 m/s, 0.207 m/s	0.562 m/s, 0.324 m/s
Inlet Turbulent Kinetic Energy, K_o	0.044 m^2/s^2	0.193 m^2/s^2 avg.
Inlet Turbulence Dissipation Rate, ε_o	0.999 m^2/s^3	3.037 m^2/s^3 avg.
Liquid Density, ρ	1000 kg/m^3	7020 kg/m^3
Liquid Laminar Viscosity, μ_o	0.001 kg/m-s	0.0056 kg/m-s
Casting Speed, V_c	Froude similarity	14.8 mm/s (35''/min)
Liquid Flow Rate (whole slab)	0.0378 m^3/min	0.376 m^3/min
Gas Flow Rate (cold) (hot)	3.71 SLPM	6.3 SLPM 34.9 SLPM
Gas Volume Fraction, f_{gas}	8.9 %	8.5%
Bubble diameter (avg)	2.43 mm	2.59 mm

To model two-phase flow, an additional set of momentum conservation equations was solved for the argon gas phase. Interphase coupling terms were added to the liquid momentum equations to account for the drag in proportion to the relative velocities of the liquid and bubble phases, which were generally in the Stokes or Allen regimes. The results depend greatly on the bubble size,[8] which in reality has a distribution that can evolve with the flow. In this work, these complex phenomena were treated by first characterizing the bubble size distribution as having eleven different discrete sizes, (0.5mm, 1.5mm, …, 10.5 mm) each with its own volume fraction, according to the Multiple Size Group model in CFX [4]. In this model, the average bubble velocity is related to the "Sauter" mean diameter of the distribution, in order to solve only a single additional set of gas momentum equations. Additional continuity equations are solved for each size group, to represent the size distribution. Furthermore, the initial bubble volume fractions, imposed at the nozzle port, were subjected to evolution, according to the binary breakup model of Luo and Svendsen [11], assuming a breakup coefficient of 0.1. Coalescence was assumed to be small (due to surface tension repulsion), by setting the coalescence coefficient [4] to 0.

The most difficult aspect of setting up the computational modeling was determination of the bubble size distribution. (Large numbers of small bubbles provide more drag than small numbers of large bubbles, so their buoyancy is able to exert more lift onto the flow pattern). The

diameters of individual bubbles were measured from still photographs of the operating water model and compiled into a volume fraction distribution. Bubble sizes in the caster were estimated by extrapolating size distributions measured in a water model of a nozzle where vertical flow generated bubbles via shear. The results were adjusted for steel / argon properties by applying the mathematical model of Bai,[6] assuming about 200 active sites for gas emission from the 78 mm bore x 50 mm high cylindrical surface area of the porous ceramic wall. The resulting size distributions for the water model and steel caster are compared in Figure 10. Bubbles in the water model are seen to have wide size variations, owing to the single, annular-shaped inlet area, which generates relatively large, elongated bubbles. The steel caster is expected to have more uniformly-sized bubbles, owing to the stable shear-driven formation mechanism expected for this low gas flow rate per pore.

The computation begins by first solving for flow in the nozzle, as shown in Figure 11. This figure illustrates how gas concentrates in the upper portion of the exit plane of the nozzle port, where the velocity, K, and ε distributions are used to define the inlet conditions for the strand simulation. The calculated flow pattern in the strand water model is compared with the velocity distribution measured using Particle Image Velocimetry in Figure 12. Both results agree that a consistent "single-roll" flow pattern is produced for these conditions, despite a few minor discrepancies with the inlet conditions. The jet is quickly buoyed up to the top surface owing to its argon gas content, and it flows along the top surface away from the SEN.

The computational model was next applied to simulate the flow pattern measured in the steel caster for approximately the same conditions. The steel caster is different from the water model in several important ways. Changes to this simulation, given in Table IV include:

-increasing the dimensions by a factor of 2.5 to simulate the full-scale geometry;
-increasing the inlet velocities by a factor of $\sqrt{2.5}$ (to simulate the actual casting speed rather than the velocities in the water model, which were scaled down according to the standard modified Froude criterion);
-replacing the domain bottom with a pressure boundary condition;
-changing the bubble distribution (Figure 10); and
-changing the liquid properties.

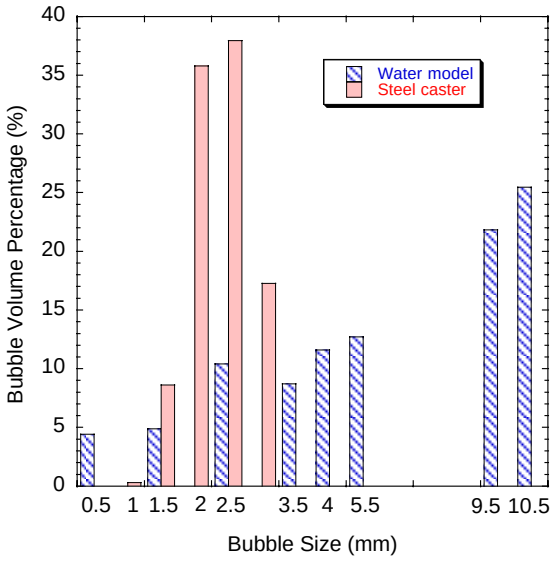

Figure 10: Bubble distributions entering water model and steel caster

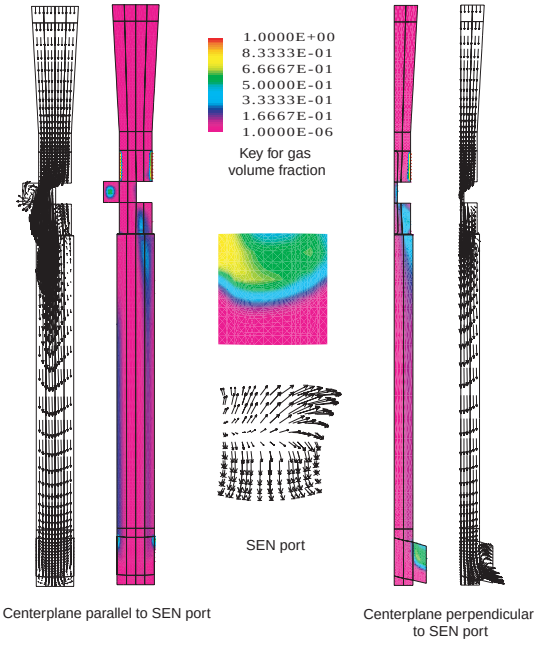

Figure 11: Computed steel velocity and gas volume fraction in nozzle

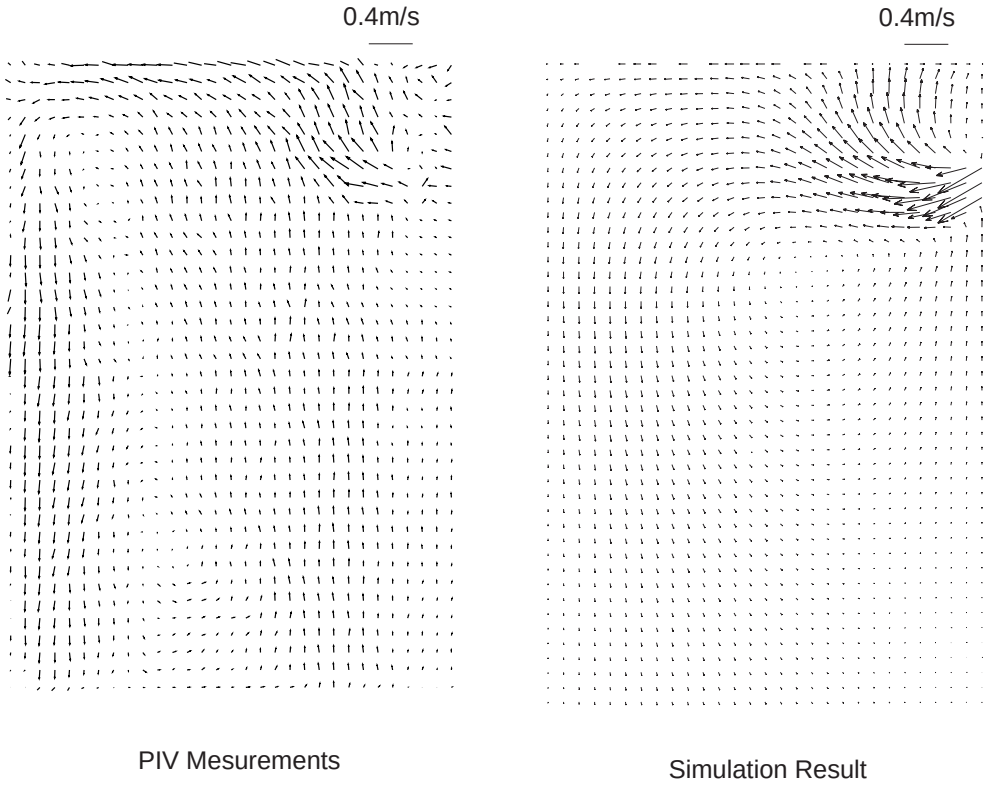

Figure 12: PIV measurements and computed velocity vectors of multiphase flow in 0.4-scale water model centerplane (Table IV conditions)

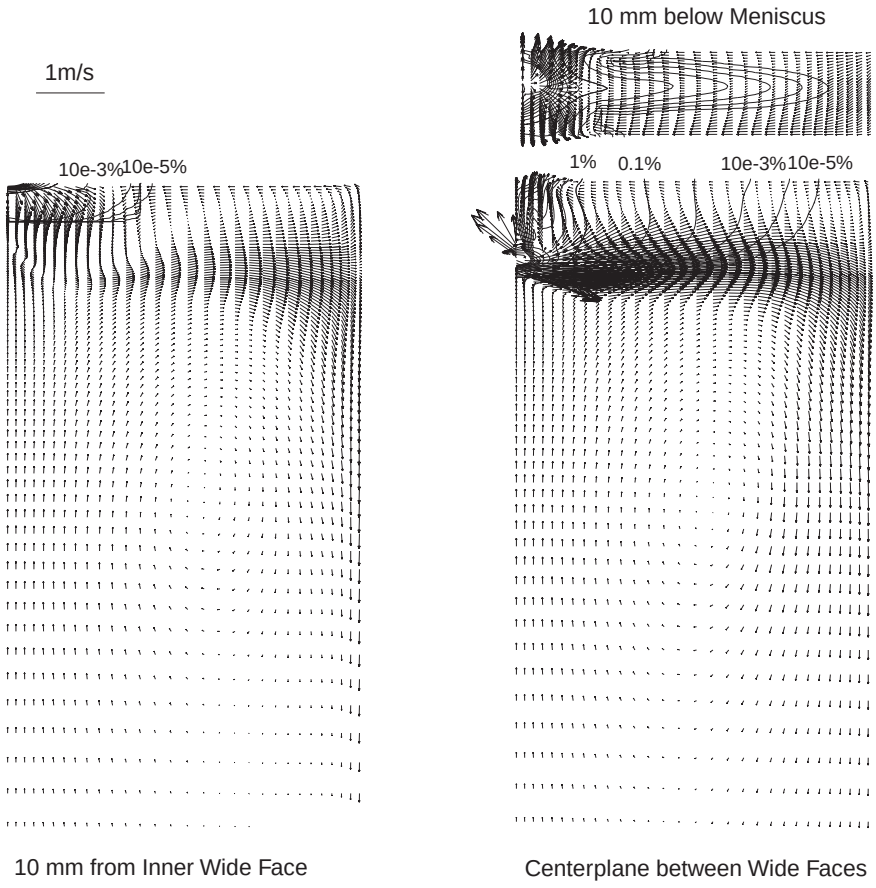

Figure 13: Computed velocities in steel caster

Figure 13 shows results for both velocity vectors and gas distribution in top view and side view slices through both the centerline and near to the wide face. The flow pattern is not symmetrical, owing to the swirling flow exiting the nozzle port that was imparted by the slide gate. The results generally exhibit classic double-roll flow behavior. The jet is quite shallow, but the flow pattern is consistently towards the SEN along the top surface. The jet first impinges on the narrow face. The bubble contours all stay within the upper recirculation zone, indicating that bubble entrapment into the lower roll should be rare. The flow pattern measured in the plant is also a double-roll flow pattern for this case,[1] which is consistent with these predictions. However, the plant measurements also show that the flow pattern sometimes experiences transition flow states, where the flow direction reversed inconsistently, and was correlated with casting defects.[1] This might be caused by transient structures breaking off from the jet, which is predicted to be quite shallow and near to the surface. Especially if the nozzle submergence becomes shallower, or if the bubble size decreased or gas fraction increased, it is not surprising from the simulation that this flow pattern might exhibit detrimental transition behavior.

The most significant finding of this study is that the flow pattern in the steel caster is sometimes very different from that in a scale water model and that the steady, multiphase K-ε computation can match both. Specifically, the flow pattern reverses from a stable single-roll flow pattern in the 0.4-scale water model to an unstable double-roll flow pattern in the full-size caster. Of the many causes for this difference, the most important is likely the reduced-scale of the water model combined with the Froude-based velocity scaling criterion. Further parametric studies with the computational model are planned to determine the upper limit for argon injection that still produces a stable double-roll flow pattern and avoids the detrimental transition flow pattern.

Acknowledgements

This work is supported by the National Science Foundation (Grant DMI-98-00274) and the member companies of the Continuous Casting Consortium at the University of Illinois at Urbana-Champaign (UIUC). The authors also wish to thank the National Center for Supercomputing Applications at UIUC and AEA Technology for computational support and the CFX software.

References

1) M. B. Assar, P. H. Dauby and G. D. Lawson:, in Steelmaking Conference Proceedings, 83, ISS, Warrendale, PA, (2000), 397-411.
2) S. Sivaramakrishnan *et. al.*:, in Ironmaking Conference Proceedings, 59, ISS, Warrendale, PA, Pittsburgh, PA, (2000), 541-557.
3) B. G. Thomas *et. al.*: *ISIJ Int.*, (2001) (in press)
4) CFX4.2: AEA Technology, 1700 N. Highland Rd., Suite 400, Pittsburgh, PA 15241, Report, (1998).
5) R. Madabushi and S. P. Vanka: *Physics of Fluids*, (1991), 3 (11), 2734.
6) H. Bai: PhD Thesis, University of Illinois, (2000).
7) R. C. Sussman, M. Burns, X. Huang and B. G. Thomas:, in 10th Process Technology Conference Proc., 10, Iron and Steel Society, Warrendale, PA, Toronto, Canada, April 5-8, 1992, (1992), 291-304.
8) B. G. Thomas, X. Huang and R. C. Sussman: *Metall. Trans. B*, (1994), 25B (4), 527.
9) L. Shiller and A. Naumann: *Ver. Deut. Ing.*, (1933), 77, 318.
10) Q. Yuan, S. P. Vanka and B. G. Thomas: *2nd International Symposium on Turbulent and Shear Flow Phenomena, June 27 - 29, 2001*, Royal Institute of Technology(KTH), Stockholm, Sweden, (2001), 6.
11) H. Luo and H.F. Svendsen: *AICHE J.*, (1996), 42 (5), 1225-1233.